

New Generation of DUV Photoresists with Precise Molecular Structure

2021 CNF Intern: Francesca Bard

Intern Affiliation: Materials Science and Engineering, Cornell University

Principal Investigator: Prof. Christopher Kemper Ober, Materials Science and Engineering, Cornell University

Mentor: Dr. Florian Hermann Ulrich Käfer, Materials Science and Engineering, Cornell University

Primary Sources of Research Funding: 2021 Cornell NanoScale Science & Technology Facility Research Experiences for Undergraduates (CNF REU) Program via National Science Foundation under Grant No. NNCI-2025233, Intel

Contact(s): fmb54@cornell.edu, c.ober@cornell.edu, fhk28@cornell.edu

Primary CNF Tools Used: ASML 300C DUV stepper, Zeiss SEM, Woollam RC2 ellipsometer, JEOL 6300

Abstract:

This CNF internship project is focused on synthesizing peptoids, with a controlled sequence of amines and chain length, to be used as photoresist materials. As photoresist materials, these peptoids must be UV sensitive, changing solubility when exposed to UV light. 10-mers (peptoids with 10 repeat units) are created with different compositions and sequences of amines to optimize the pattern resolution of the photoresist. These positive tone chemically amplified photoresists are exposed with deep ultraviolet (DUV) to create line patterns ranging from 1-0.1 μm . The line patterns are analyzed to determine the effect of the chosen composition and sequence.

Summary of Research:

Introduction. Photoresists are typically made of polymers that are polydisperse and whose monomers are randomly distributed along the chain. These attributes bottleneck the ability to attain smaller feature sizes since the dispersity and length affects photoresist properties. Therefore, it is imperative to create new materials where the sequence and chain length can be controlled, like peptoids.

Peptoid Synthesis and Characterization. The peptoids are synthesized by adding each amine to 2-chlorotrityl chloride resin through bromoacetylation and displacement until all ten amines (R groups) are added. (see Figure 1).

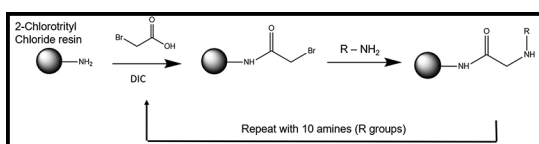


Figure 1: Peptoid synthesis on 2-chlorotrityl chloride resin through bromoacetylation and displacement until all ten amines (R groups) are added.

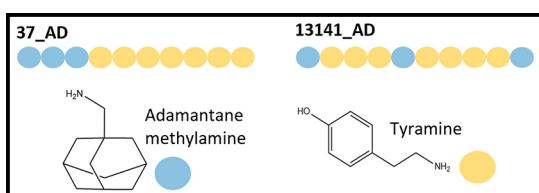


Figure 2: Peptoid amine sequence of samples 37_AD and 13141_AD.

This process repeats until all 10 amines are added to the chain. The samples have different sequences but the same composition — 3 adamantane methylamine (AD) and 7 tyramine (TA). Sample 37_AD has sequence AD₍₃₎-TA₍₇₎, and sample 13141_AD has sequence AD₍₁₎-TA₍₃₎-AD₍₁₎-TA₍₄₎-AD₍₁₎ (see Figure 2).

Afterward, the peptoids are cleaved off the resin using mild acid, protected, and purified. The amine, tyramine, present in all samples, is protected using di-*tert*-butyl dicarbonate. Exposure to UV light deprotects tyramine, changing its chemical structure and solubility. The samples are then purified using preparative high-performance liquid chromatography (HPLC). The glass transition temperature of the peptoids is determined through differential scanning calorimetry (DSC), and the mass is verified through liquid chromatography-mass spectrometry (LC-MS).

Exposures. For spin coating, the peptoids are dissolved in organic solvent and a photoacid generator is added. The solution is then sonicated and filtered to degas before spin coating on a silica wafer. The wafer is baked (pre and post) at the glass transition temperature of the peptoids. The wafer is then exposed using the ASML 300C DUV stepper to print line and resolution patterns.

Solubility and SEM Images. Following exposures, the film is tested for different developers at various times to remove the exposed/unprotected regions on the film. To optimize contrast, there must be a great difference in solubility before (protected) and after exposures (unprotected). The

solubility before and after exposures differ between the two samples (see Figure 3). After developing the film, the patterns are observed and analyzed using scanning electron microscopy (SEM). As shown in Figure 4, these peptoids produce clear patterns smaller than $0.4 \mu\text{m}$, which is already approaching the limits of DUV lithography ($0.2 \mu\text{m}$). After being developed in ethyl acetate for 45 seconds, 13141_AD produced clear line patterns of $0.4 \mu\text{m}$. Sample 37_AD was developed in ethyl acetate for two minutes and produced clear line patterns of $0.3 \mu\text{m}$.

Conclusions and Future Steps:

Although these samples have the same composition, their solubility is different before and after exposures. This suggests that the sequence of amines influences solubility and contrast, and is thus an important factor when optimizing the photolithography performance. Patterns this small (0.4 and $0.3 \mu\text{m}$) and clear are promising results for even smaller feature sizes that are possible to print with e-beam and extreme ultraviolet (EUV) exposures. We will perform e-beam exposures with the JEOL 6500 and EUV exposures with Intel. Furthermore, to have greater control over the placement of the photoacid generators, we will be including a photoacid generator as one of the amines of the 10-mer. This will guarantee a more homogenous film and distribution of the photoacid generator.

Acknowledgments:

I would like to thank Dr. Florian Käfer, the rest of the Ober group, and the CNF staff for their support this summer. This work was performed in part at the Cornell Center for Materials Research (CCMR) and at Cornell NanoScale Science & Technology Facility (CNF), a member of the National Nanotechnology Coordinated Infrastructure (NNCI), which is supported by the National Science Foundation (Grant NNCI-2025233). I would like to thank Intel for also funding this research.

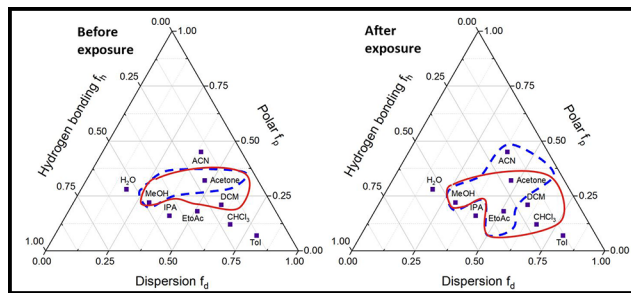


Figure 3: TEAS plots showing the solubility for samples 37_AD (blue dotted lines) and 13141_AD (red solid lines) before and after exposures.

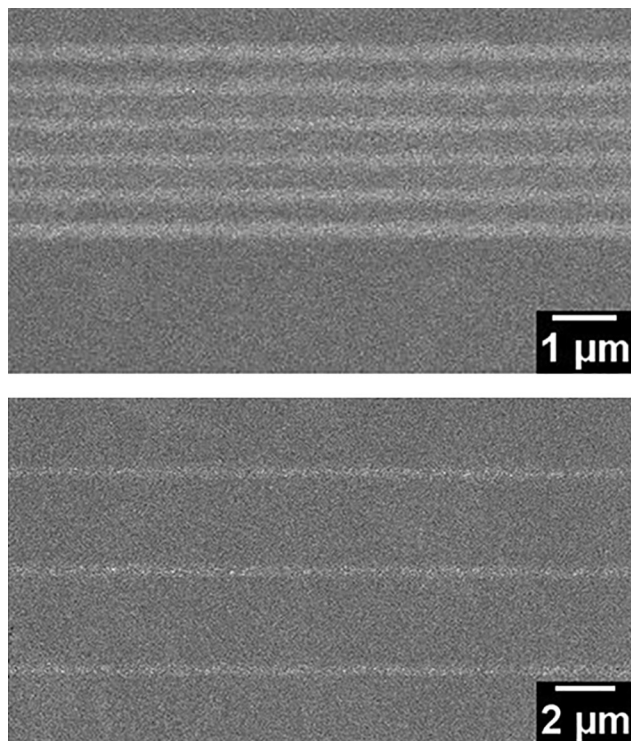


Figure 4: SEM images of line space patterns of (top) 37_AD and (bottom) 13141_AD; developed in ethyl acetate for two minutes and 45 seconds, respectively.

A New Generation of Small Molecules for EUV Photolithography

2021 CNF REU Intern: Kareena Dash

Intern Affiliation: Biological Sciences, Chemistry, Cornell University

CNF REU Principal Investigator: Professor Christopher Kemper Ober, Materials Science and Engineering, Cornell University

CNF REU Mentor: Dr. Florian Hermann Ulrich Käfer, Materials Science and Engineering, Cornell University

Primary Source of Research Funding: 2021 Cornell NanoScale Science & Technology Facility Research Experiences for Undergraduates (CNF REU) Program via National Science Foundation under Grant No. NNCI-2025233, Intel

Contact(s): kd366@cornell.edu, c.ober@cornell.edu, fhk28@cornell.edu

Primary CNF Tools Used: ASML 300C DUV stepper, JEOL 6300 electron-beam, Zeiss Ultra SEM, RC2 Woollam ellipsometer

Abstract:

Modern computer chips require smaller and smaller feature sizes in the 3 to 5 nm range to reach greater efficiencies. One way to achieve this is by using polymeric resists with well-defined repeat group sequences. In this research, peptoids, made of amine monomers, have been synthesized to contain identical sequences and very small chain sizes in a specific sample, allowing for higher pattern resolution. Azide-alkyne click chemistry has been used on the peptoid backbone to homogeneously introduce new functionalities to the peptoid. Peptoids of two different sequences were synthesized, and the photolithographic properties were investigated through deep ultraviolet (DUV) and electron-beam photolithography exposures.

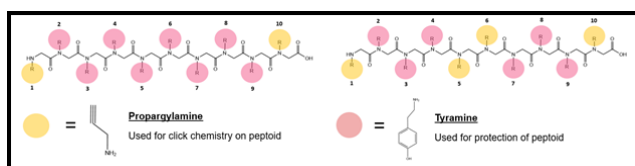


Figure 1: Chosen sequences for peptoid samples, 181-ProT on left and 13231-ProT on right.

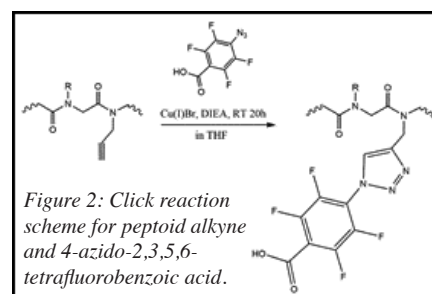


Figure 2: Click reaction scheme for peptoid alkyne and 4-azido-2,3,5,6-tetrafluorobenzoic acid.

Summary of Research:

In this work, we utilize click chemistry on a small, sequence-controllable molecule, called a peptoid, to generate a new polymeric photoresist material. Click chemistry is a category of highly specific, high yield, fast reactions that form a bond between two particular chemical handles [1].

Two peptoids were synthesized to contain 10 units of different compositions of propargylamine (Pro) and tyramine (Tyr). The sequences were 181-ProT and 13231-ProT (Figure 1). The alkyne group of propargylamine served as a click handle, whereas tyramine was protected for photolithography exposures. The peptoid synthesis was performed using repeated acylation and replacement steps on 2-chlorotriptyl chloride resin. The peptoid was cleaved from the resin and protected using di-tert-butyl dicarbonate.

For the click reaction, 1 equiv. of protected peptoid was stirred with 40 equiv. *N,N*-diisopropylethylamine, 2 equiv. Cu(I)Br, and 5 equiv. of 4-azido-2,3,5,6-tetrafluorobenzoic acid (Azo4FBA) in tetrahydrofuran (THF) for 20 hr at room temperature [2] (Figure 2). The fluorinated azido-acid was chosen for the purpose of increasing hydrophobicity of the resist and providing the first step for a homogeneously distributed photoacid generator.

The peptoid samples were characterized by differential scanning calorimetry (DSC), matrix-assisted laser desorption/ionization-time of flight (MALDI-TOF), and nuclear magnetic resonance (NMR) spectroscopy. With DSC, the glass transition temperature of 181-ProT was determined to be 120°C. Through MALDI-TOF, the

theoretical mass of 181-ProT (2425.14 g/mol) was found, verifying the synthesis of the correct peptoid product. $^1\text{H-NMR}$ of 181-ProT and 181-ProT-Clicked showed the disappearance of an alkyne-indicative proton peak around 3.03 ppm, while $^{19}\text{F-NMR}$ data for 181-ProT-Clicked displayed a peak around -75 ppm, proving the successful clicking of Azo4FBA. The resist performance was determined through DUV and electron beam photolithography. Isopropanol was found to be the most effective developer for both sets of samples, 181-ProT and 13231-ProT, at a developing time of one minute. The RC2 Woollam ellipsometer was utilized to measure the film thickness of each box on the 181-ProT flat exposure to determine the best dose for DUV photolithography. Scanning electron microscopy (SEM) images were taken of the DUV line-space pattern and electron beam samples for further characterization.

This work found that adjusting the sequence of propargylamine and tyramine monomers changes the solubility and performance of the resist. Clear DUV and electron beam line-space patterns were observed (Figures 3 and 4), signifying good resolution. Additionally, the successful peptoid azide-alkyne cycloaddition indicates that click reactions allow easy modification of peptoid resist properties. In the future, new azides with different functionalities will be clicked on Pro-Tyr peptoids to alter resist properties such as solubility, glass transition temperature, and resist performance. Altogether, this research has explored a promising avenue for polymeric photoresist development for EUV photolithography.

Acknowledgements:

The author would like to thank the National Science Foundation, NNCI, and Cornell NanoScale Science & Technology Facility Research Experiences for Undergraduates (CNF REU) Program (NSF grant no. NNCI-2025233). Thank you to Professor Christopher Ober, Dr. Florian Käfer, the whole Ober research group, and the CNF REU Program Coordinator and Staff. Thank you to Intel for also funding this research.

References:

- [1] Castro, V.; Rodríguez, H.; and Albericio, F. CuAAC: An Efficient Click Chemistry Reaction on Solid Phase. *ACS Comb. Sci.* 2016 18 (1), 1-14.
- [2] Thundimadathil, J. Click Chemistry in Peptide Science: a Mini-Review. *Chimica Oggi -Chemistry Today.* 2013 31 (2), 34-37.

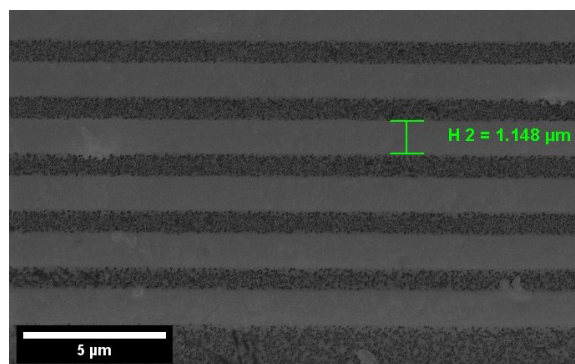


Figure 3: SEM image of 1.15 μm line pattern from DUV exposure on 181-ProT.

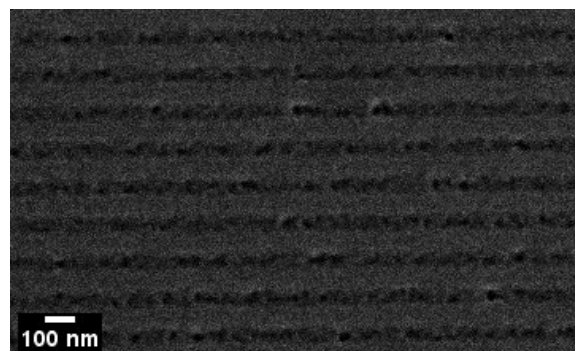


Figure 4: SEM image of 83 nm line pattern from e-beam exposure on 13231-ProT.

Mesoporous Thin Film Quantum Materials via Block Copolymer Self-Assembly Patterned by Photolithography

CNF Project Number: 1356-05

Principal Investigator(s): Ulrich Wiesner

User(s): Fei Yu, R. Paxton Thedford

Affiliation(s): Department of Materials Science and Engineering, Cornell University

Primary Source(s) of Research Funding: U.S. Department of Energy (DOE),
Office of Science (Basic Energy Sciences (DE-SC0010560))

Contact(s): ubw1@cornell.edu, fy84@cornell.edu

Website: <http://wiesner.mse.cornell.edu/>

Primary CNF Tools Used: Oxford 81 etcher, VersaLaser engraver/cutter tool, ABM contact aligner

Abstract:

The use of block copolymers (BCPs) as structure directing or templating agents, offers facile pathways toward quantum metamaterials with highly tunable mesostructures via scalable solution processing. Here, we report the preparation of mesoporous niobium carbonitride-type thin film superconductors through spin-coating of a hybrid solution containing an amphiphilic BCP swollen by niobia sol precursors and subsequent thermal processing in combination with photolithography. Spin-coated as-made BCP-niobia hybrid thin films on silicon substrates after photolithographic definition are heated in air to produce a porous oxide, and subsequently converted to carbonitrides via high temperature treatment in reactive gases including ammonia. Electrical transport measurements show initial exponential rise in resistance before dropping to zero into a superconducting state. Such cost-effective and scalable solution-based quantum materials fabrication approaches may be integrated into existing microelectronics processing, combining the capabilities of soft matter self-assembly with quantum materials.

Summary of Research:

The general solution-based fabrication route toward NbCN-type thin films on silicon substrates is depicted in Figure 1, based upon past efforts to synthesize similar materials in the bulk [1]. The structure-directing BCP in the study is an amphiphilic triblock terpolymer poly(isoprene-*b*-styrene-*b*-ethylene oxide) (PI-*b*-PS-*b*-PEO, referred to as ISO hereafter), synthesized by sequential anionic polymerization. The inorganic niobia sol precursor is prepared from the hydrolytic condensation of niobium (V) ethoxide. Upon mixing the sol with ISO in tetrahydrofuran (THF) and subsequent spin-coating and self-assembly (Figure 1a,b), the niobia sol particles selectively mix with the hydrophilic PEO block of the ISO to form a nanostructured composite thin film. Without post-deposition annealing such as solvent vapor annealing, the hybrid films are treated in air at 450°C to further condense the niobia and remove the structure directing ISO. The resulting niobium oxide thin films (Figure 1c) show locally ordered mesoporous structures, and subsequent treatment in ammonia at 700°C yields metallic niobium oxynitride thin films (Figure 1d). Finally, treatment in carburizing gas at 1000°C yields superconducting niobium carbonitride thin films (Figure 1e). Photolithography (Figure 1f-k) is used to pattern the thin films for further processing.

Without post-deposition annealing such as solvent vapor annealing, the hybrid films are treated in air at 450°C to further condense the niobia and remove the structure directing ISO. The resulting niobium oxide thin films (Figure 1c) show locally ordered mesoporous structures, and subsequent treatment in ammonia at 700°C yields metallic niobium oxynitride thin films (Figure 1d). Finally, treatment in carburizing gas at 1000°C yields superconducting niobium carbonitride thin films (Figure 1e). Photolithography (Figure 1f-k) is used to pattern the thin films for further processing.

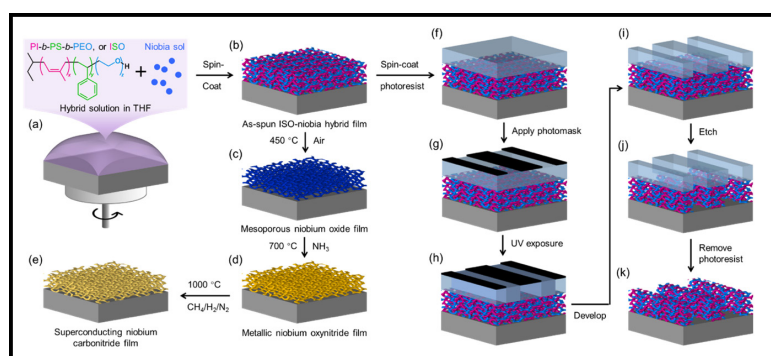


Figure 1: Schematic of solution-based fabrication processes. (a) ISO and niobia sol hybrid solution in THF is spin-coated on a silicon substrate. (b) As-spun ISO-niobia hybrid thin film. (c) Mesoporous niobium oxide thin film after heating in air at 450°C. (d) Metallic niobium nitride thin film after treatment in ammonia at 700°C. (e) Superconducting niobium carbonitride-type thin film after final treatment in carburizing gas at 1000°C. (f) – (k) Photolithography route to patterned thin films that can be further processed along (c) to (e).

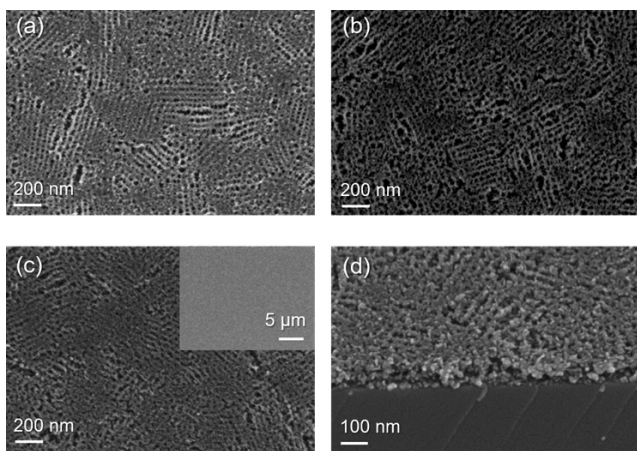


Figure 2: SEM images of thin films at different processing stages. Plan views of (a) the niobium oxide film; (b) the niobium nitride film; (c) the niobium carbonitride film (inset at low magnification). (d) 45-degree cross-sectional view of the niobium carbonitride film displaying the film edge on the cleaved silicon substrate.

as evidenced by scanning electron microscopy (SEM, Figure 2a). X-ray scattering suggests the morphology is consistent with a deformed alternating gyroid structure, in which the niobia in the original hybrid film is retained as a single inorganic minority network replicating the PEO plus inorganic. To render the thin films electrically conducting, a nitridation step in ammonia (NH_3) at 700°C converts the mesoporous oxide into niobium nitride (NbN, Figure 1d), albeit with some oxygen (and vacancies) likely remaining. The mesostructure appears largely unchanged, with a slight coarsening of the nodes in the network (Figure 2b).

Finally, heating the NbN thin films to 1000°C in a mixture of methane (CH_4), hydrogen (H_2), and nitrogen (N_2), known as carburizing gas ($\text{CH}_4/\text{H}_2/\text{N}_2$), yields a superconducting niobium carbonitride (NbCN)-type material (Figure 1e) without substantial further growth in crystallite size. The overall mesoporous structure is retained, albeit with additional coalescence of struts (Figure 2c). With the simple spin-coating technique, a uniform thin film with arbitrary lateral dimensions can be fabricated without major macroscopic defects (inset of Figure 2c).

Photolithography was performed to illustrate compatibility of our solution-based synthesis approaches to mesoporous superconducting samples with typical semiconductor nanofabrication processing (Figure 1f-k).

First, a photoresist is applied on the ISO-niobia hybrid thin films pre-treated at 300°C to minimize swelling or dissolution by photoresist solution. After exposure using the ABM contact aligner and development, $25\ \mu\text{m}$ wide strips of photoresist layers are removed. Pattern transfers are achieved by a combination of wet etching using buffered oxide etchant (BOE) and dry etching using oxygen plasma. The clear and sharp patterns demonstrate the viability for

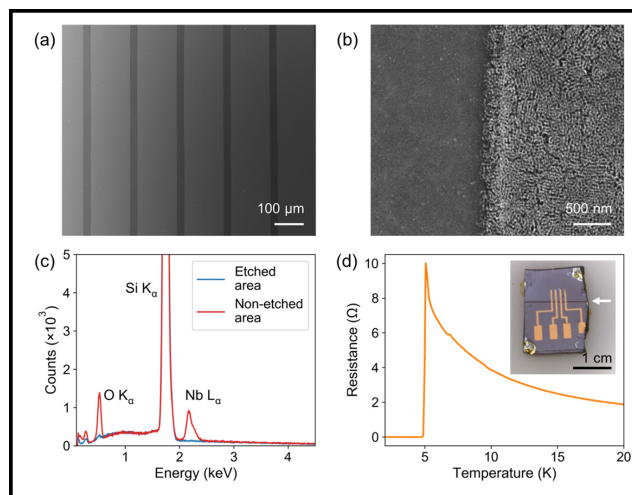


Figure 3: Lithographic patterning of spin-coated thin films. (a) Plan-view SEM image of niobium carbonitride thin film patterned through photolithography, with $25\ \mu\text{m}$ wide strips etched away shown in dark. (b) Higher magnification SEM image of the patterned film showing the edge along with details of the self-assembled mesostructure. (c) EDS spectra of areas of plain film and etched film after 10-min CF_4 plasma etching. (d) Plot of resistance versus temperature from an individual patterned $400\ \mu\text{m}$ wide strip thin film. Inset shows the single lithographically patterned niobium carbonitride strip (white arrow) with four co-linear metal contacts across the strip.

the superconducting thin films based on solution processing to be incorporated into standard microelectronic processing, with additional self-assembled 3D features at the mesoscale (Figure 3a,b).

A separate pattern was transferred from a shadow mask (fabricated using the VersaLaser engraver/cutter tool) through CF_4 plasma etching using the Oxford 81 Etcher. The CF_4 plasma etching can completely remove the ISO-niobia hybrid materials, as evidenced by the disappearance of the Nb La peak in energy-dispersive X-ray spectroscopy (EDS) spectra (Figure 3c). Films patterned via plasma etching (Figure 3d, inset, white arrow) have a superconducting transition temperature of 5 K (Figure 3d).

In summary, our work opens pathways toward solution-based thin film technologies at the intersection between soft matter self-assembly and quantum materials with tremendous academic as well as industrial potential.

References:

- [1] Beaucage, P. A.; Van Dover, R. B.; DiSalvo, F. J.; Gruner, S. M.; Wiesner, U. B. Superconducting Quantum Metamaterials from Convergence of Soft and Hard Condensed Matter Science. *Adv. Mater.* 2021, 33, 2006975.
- [2] Yu, F.; Thedford, R. P.; Hedderick, K. R.; Freychet, G.; Zhernenkov, M.; Estroff, L. A.; Nowack, K. C.; Gruner, S. M.; Wiesner, U. B. Patternable Mesoporous Thin Film Quantum Materials via Block Copolymer Self-Assembly: An Emergent Technology? *ACS Appl. Mater. Interfaces* 2021, ASAP, DOI: 10.1021/acsami.1c09085.

Nano-Scale Area-Selective Formation of Polymer Brushes

CNF Project Number: 1757-09

Principal Investigator(s): Christopher Kemper Ober

User(s): Yuming Huang

Affiliation(s): Department of Materials Science and Engineering, Cornell University

Primary Source(s) of Research Funding: National Science Foundation

Contact(s): cko3@cornell.edu, yh839@cornell.edu

Website: <https://ober.mse.cornell.edu/index.html>

Primary CNF Tools Used: E-beam resist spinners, JEOL 9500, FilMetrics F50-EXR, Oxford 81 etcher, Zeiss Ultra SEM, optical microscope, Oxford 81

Abstract:

Polymer brushes can be formed in a location-specific manner via an integrated fabrication of surface-initiated polymerizations and electron-beam lithography, which is a state-of-art patterning tool known for its fine resolution and precision. Dot-patterned polymer brushes was produced on silicon wafers by area-selective deposition of initiators, using patterned e-beam resists as the masks. As a result, “nano-spikes” made of polypeptide (rod) brushes and “blurry bundles” of polystyrene (coil) brushes were formed via two different kinds of surface-initiated polymerizations. This platform can be useful for various applications such as cytoskeleton mimicry and molecular recognition.

Summary of Research:

Introduction. Polymer brushes are polymer chains that have one end covalently anchored to a flat substrate, such as a silicon wafer, with a high grafting density. Due to the unusual molecular arrangements and surface attachments, polymer brushes have exhibited unique surface properties and thus has an active research area in polymer science [1]. Potential applications such as organic thin film devices, optoelectronics, and medical diagnosis have been studied in the past decades. However, there is an increasing need for area-selective functionalization of metal oxide surfaces (for e.g. device fabrications) as lithographic techniques and nanofabrication advance. As such, making nanopatterned polymer brushes by incorporating e-beam lithography with the vapor phase surface-initiated polymerization can be one possible solution to these demands.

In addition to the polypeptide brushes, we have fabricated different polymer brushes by utilizing a new type of living polymerization into the integrated process, which will widen the potential of surface functionalities as well as fundamental studies of polymer brushes.

Fabrication. The polymer brushes were patterned on a silicon wafer via an integrated fabrication process and area-selective deposition of surface-bound initiators for polymerizations.

E-Beam Resist Mask Preparation. Patterned e-beam resist mask (~150 nm) was prepared through JEOL 9500. The sample was then etched ~ 40 nm using the Oxford 81 etcher to remove residual debris in the unmasked area.

Synthesis of the Rod Brushes. The deposition of a silane initiator on the treated substrate was carried out in a closed chamber under vacuum and elevated temperature. The initiator was allowed to vaporize and thus react with the exposed metal oxide surfaces. Afterward, the resist mask was removed by organic solvents. Subsequently, surface-initiated ring-opening polymerization of poly- γ -benzyl-L-glutamate (PBLG), a rod-like polymer, was synthesized under vacuum and elevated temperature.

Synthesis of the Coil Brushes. After the deposition of silane initiator, there was one additional step of modifying these surface initiators with allyl 2-bromo-2-methylpropionate (BiBB), which acts as the activation site for the subsequent polymerization. Polystyrene (PS), a coil-like polymer, was then synthesized via surface-initiated Cu(0) mediated controlled radical polymerization (SI-CuCRP) under argon-protected environment and elevated temperature. Similar process was also carried out for other coil brushes such as poly(methyl methacrylate) (PMMA) to test the fabrication's adaptability.

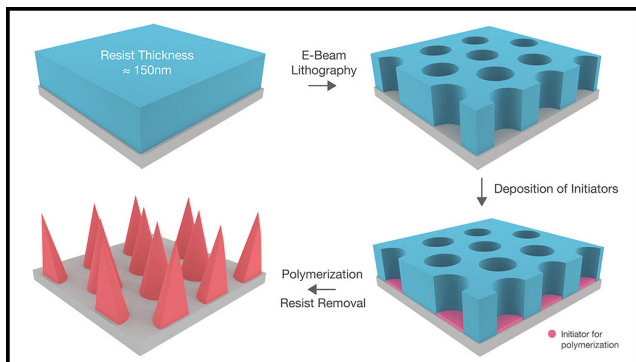


Figure 1: Schematic illustration of the fabrication process.

A schematic illustration of the whole fabrication process is shown in Figure 1.

Characterization and Results:

The e-beam resist thickness was measured by FilMetrics F50-EXR. The patterned e-beam resist (Figure 2), the patterned PBLG brushes (Figure 3) and PS brushes

(Figure 4) were characterized using Zeiss Ultra scanning electron microscopy (SEM) and Veeco Icon Atomic Force Microscope (AFM) for topological analysis.

Conclusion and Future Steps:

In conclusion, we demonstrated a novel process for precisely control the spatial arrangement of different kinds of polymer brushes. In the near future, we plan to examine how the surface topography varied with different kind of polymers in terms of molecular structures and physical properties. We also plan to explore the use of these surfaces for various applications, such as cell membrane support, biological simulated model and magnetic storage platforms.

References:

- [1] Chen, W. L.; Cordero, R.; Tran, H.; Ober, C. K., 50th Anniversary Perspective: Polymer Brushes: Novel Surfaces for Future Materials. *Macromolecules* 2017, 50 (11), 4089-4113.
- [2] Zhang, T.; Du, Y.; Müller, F.; Amin, I.; Jordan, R., Surface-initiated Cu(0) mediated controlled radical polymerization (SI-CuCRP) using a copper plate. *Polym Chem-Uk* 2015, 6 (14), 2726-2733.

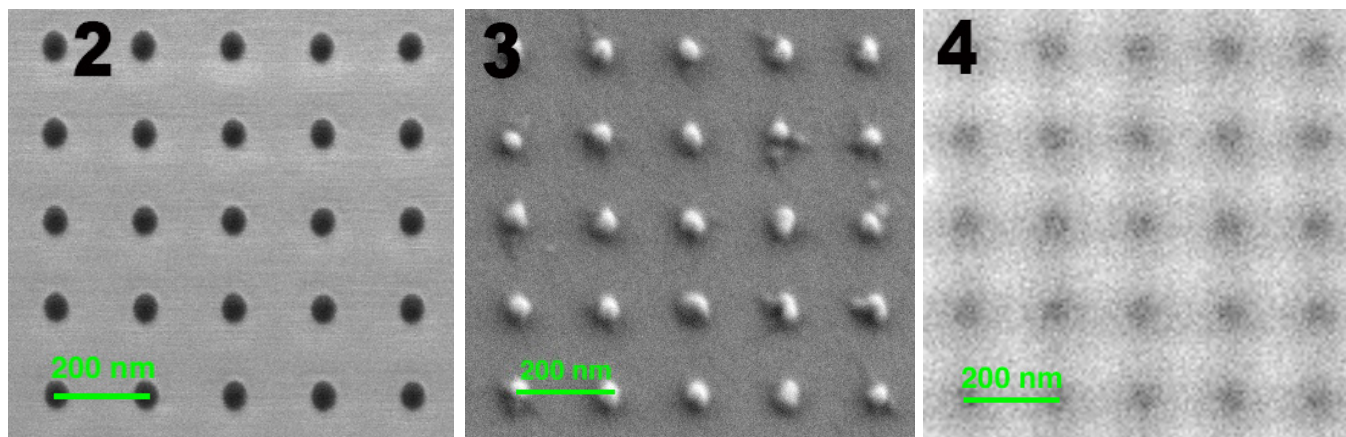


Figure 2, left: SEM of patterned e-beam resist. Figure 3, middle: SEM of the patterned PBLG rod brushes. Figure 4, right: SEM of the patterned PS brushes.

Raman Spectroscopy and Aging of the Low-Loss Ferrimagnet Vanadium Tetracyanoethylene

CNF Project Number: 2126-12

Principal Investigator(s): Gregory D. Fuchs¹

User(s): Hil Fung Harry Cheung², Michael Chilcote²

Affiliation(s): 1. School of Applied and Engineering Physics, 2. Department of Physics; Cornell University

Primary Source(s) of Research Funding: Department of Energy (Grants No. DE-SC0019250)

Contact(s): gdf9@cornell.edu, hc663@cornell.edu, mac578@cornell.edu

Website: <http://fuchs.research.engineering.cornell.edu>

Primary CNF Tools Used: GCA 5x stepper, AJA sputtering deposition system, P10 profilometer, Westbond 7400A ultrasonic wire bonder

Abstract:

Vanadium tetracyanoethylene ($V[TCNE]_x$, $x \sim 2$) is a low loss organic-based ferrimagnet with a magnetic ordering temperature $T_C > 600$ K and growth compatibility with many substrates. These properties make it an attractive candidate for coherent magnonics and quantum transduction applications. However, like other organic materials, it is sensitive to air. Encapsulation extends its lifetime in ambient conditions from hours to weeks, but its aging mechanism is not well understood. Here we report micro-focused Raman spectroscopy of $V[TCNE]_x$ as it ages to understand the structural changes accompanying aging and the corresponding changes in magnetism. We also study laser-induced degradation, which enables laser patterning by removing magnetism. These findings enable a local optical probe of $V[TCNE]_x$ quality when local magnetization characterization is impossible, and they enable a new form of patterning.

Summary of Research:

$V[TCNE]_x$ is an organic-based material with low magnetic damping comparable to that of yttrium iron garnet (YIG) at room temperature [1]. It can be grown on a variety of substrates and is an attractive alternative to YIG for coherent magnonics applications. One challenge of working with $V[TCNE]_x$ is its air sensitivity. While encapsulation extends its lifetime from hours to weeks, its aging mechanism is not well understood.

In this work we use a combination of confocal microscopy, micro-focused Raman spectroscopy, ferromagnetic resonance (FMR) and *ab initio* calculations to study $V[TCNE]_x$ and its aging mechanisms [2].

We characterize $V[TCNE]_x$ using Raman spectroscopy to study its structure. By comparing the spectrum with density functional theory (DFT) calculations, we assign the experimental Raman peaks to V-N (336, 457, 543 cm^{-1}), C=C (1308, 1411, 1530 cm^{-1}), C≡N (2121, 2194, 2214 cm^{-1}) vibrational modes (Figure 1). These Raman peaks reflect the bonding between vanadium ion and TCNE group and are relevant for magnetism.

Having characterized a pristine $V[TCNE]_x$ film, we next study the effects of aging by laser-induced damage. This allows us to study the effect of aging in the absence of diffused oxygen and water. The response of $V[TCNE]_x$ under high intensity light is particularly relevant for quantum applications requiring coupling between $V[TCNE]_x$ and defect centers [3]. Under focused laser illumination, the sample shows an increase in photoluminescence, which we characterized by a laser damage susceptibility χ_{PL} . This laser damage susceptibility increases with laser power, indicating that the damage is not a single photon process (Figure 2). Instead, this suggests it is a heating effect, where chemical reaction rate increases nonlinearly with temperature.

Next we examine the Raman spectra after the sample has been laser damaged. Raman intensity near 2121 cm^{-1} reduces while intensity near 2202, 2225 cm^{-1} increases. Peaks near 1308, 1530 cm^{-1} increases in intensity and linewidth. Low wavenumber peaks (300-600 cm^{-1}) vanishes. These features

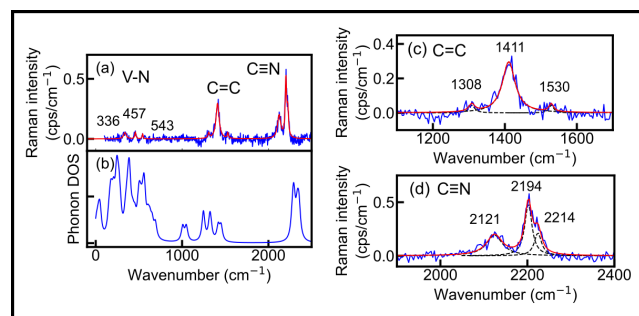


Figure 1: (a) Experimental $V[TCNE]_x$ Raman spectrum. (b) Ab initio density functional theory (DFT) calculated density of states where each mode is broadened as a Lorentzian with a full width half maximum (FWHM) of 20 cm^{-1} . (c) C=C, (d) C≡N peaks. Individual Lorentzian fits (dashed).

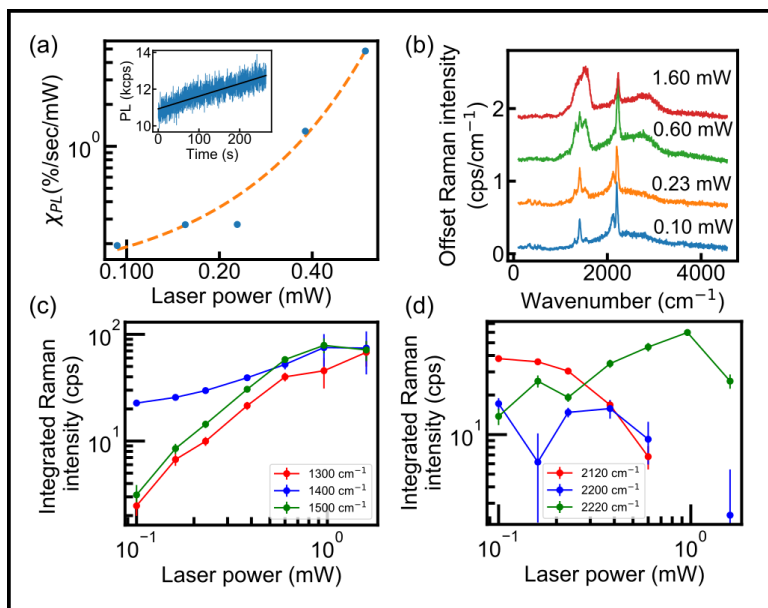


Figure 2: (a) Laser damage susceptibility increases with optical power. (Dashed) A guide to the eye showing an exponential dependence with optical power. (Inset) Photoluminescence over time and a linear fit. (b) Raman spectra at different optical power. (c), (d) Integrated intensity from individual Raman peaks for C=C and C=N peaks.

are clear signatures of aging and suggest a reduction in bonding between vanadium and TCNE. This may reduce spin exchange and magnetization.

We next study V[TCNE]_x aging at room temperature in ambient atmosphere. One clear visual signature of aging is the film turning from opaque to transparent, as shown in Figure 3 where the transparency front advances from sample edges to the center, which we attribute to diffused oxygen and water across the encapsulation epoxy. In comparison, the central region does not show a strong color change, suggesting it has not been oxidized. We observe similar changes in Raman spectra for both a laser damaged sample and a naturally aged sample, indicating similar reactions are happening in both processes. A more drastic signature of aging is the increase in laser damage susceptibility χ_{PL} , which increases exponentially in time while the effective magnetization reduces over time. This establishes a link between optical properties and magnetic properties and show that optical measurement can be a local probe of V[TCNE]_x film quality.

With the findings of V[TCNE]_x laser damage, we explore using it for patterning by selectively damaging V[TCNE]_x to remove magnetism. We show a proof-of-concept demonstration by writing the collaboration's affiliations on a V[TCNE]_x film (Figure 4). Laser damaged regions have a higher photoluminescence. This also turns the material transparent which appears bright in the optical micrograph.

This work shows optical measurement can be used to assess V[TCNE]_x film quality. In the future, we plan to study the anisotropy and spin wave modes of patterned V[TCNE]_x.

References:

- [1] H. Yu, et al. "Ultra-Narrow Ferromagnetic Resonance in Organic-Based Thin Films Grown via Low Temperature Chemical Vapor Deposition" Applied Physics Letters 2014, 105, 012407.
- [2] H. F. H. Cheung, et al. "Raman Spectroscopy and Aging of the Low-Loss Ferrimagnet Vanadium Tetracyanoethylene" 2021, arXiv:2101.10240.
- [3] D. R. Candido, et al. "Predicted Strong Coupling of Solid-State Spins Via a Single Magnon Mode" Materials for Quantum Technology 2020, 1, 011001.

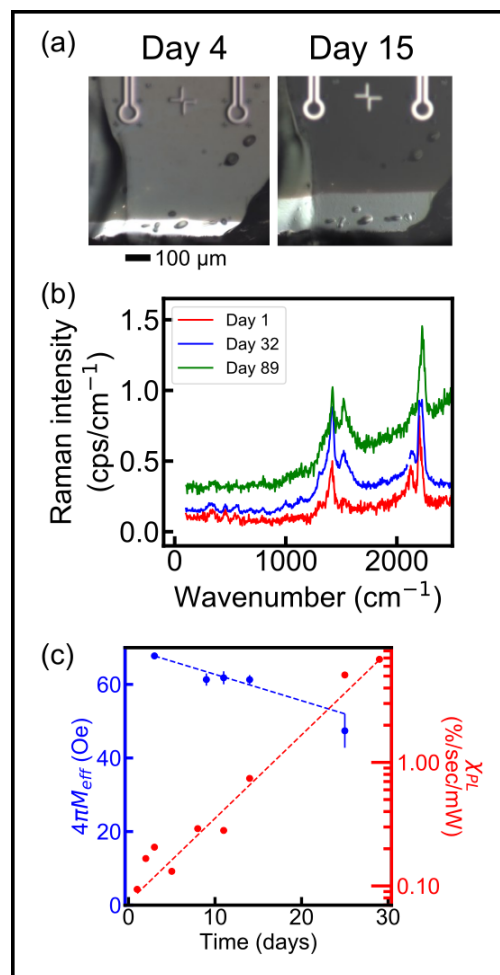


Figure 3: (a) Visual indication of aging, where the transparency front advances from sample edges to the center, revealing the underlying reflective aluminum layer. (b) Raman spectra without baseline subtraction at the central region. Fluorescence background increases and peaks at 1300, 1500 cm⁻¹ (C=C) increases. Low wavenumber (300-600 cm⁻¹, V-N) and 2120 cm⁻¹ (C=N) peaks vanish. (c) A reduction in the effective magnetization $4\pi M_{eff}$ and an increase in laser damage susceptibility. Fitted decay rate of 0.72 Oe/day and laser damage susceptibility increases with a 1/e time constant of 6.4 days.

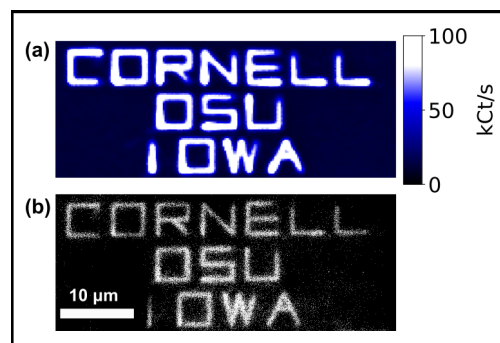


Figure 4: Laser patterning of a 400 nm V[TCNE]_x film. (a) Photoluminescence map of the patterned sample. High photoluminescence regions are laser damaged. (b) Optical micrograph. Laser damaged regions are more transparent and appear brighter in this image.

Encapsulation of Photocathodes in Two-Dimensional Materials

CNF Project Number: 2584-17

Principal Investigator(s): Melissa A. Hines

User(s): Qingyuan “Amy” Zhu, Dulanga Somaratne

Affiliation(s): Department of Chemistry and Chemical Biology, Cornell University

Primary Source(s) of Research Funding: Center for Bright Beams, an NSF Science and Technology Center

Contact(s): Melissa.Hines@cornell.edu, qz337@cornell.edu, dulanga.somaratne@cornell.edu

Website: <http://hines.chem.cornell.edu>

Primary CNF Tools Used: CVC SC4500 odd-hour evaporator, Glen 1000 resist strip

Abstract:

We are developing a new technique for encapsulating highly reactive photocathodes in an atomically thin membrane that protects them from oxidation and degradation without affecting their photoemission properties or chemical purity.

Summary of Research:

Photocathodes are materials that eject electrons under illumination. By their very nature, high-performance photocathodes must be made from materials that lose electrons easily — in other words, materials that are easily oxidized. For example, many photocathodes are either coated with alkali metals (e.g., Cs/GaAs) or comprised of alkali metals (e.g., Cs₃Sb). This presents a technical challenge, as exposure to even trace amounts of O₂ or H₂O will destroy or degrade the photocathode. For highest performance, the photocathodes must also be atomically flat and extremely homogeneous.

To meet these challenges, we are developing a technique to produce photocathodes encapsulated in two-dimensional materials, such as graphene or hexagonal boron nitride. The key challenge in this project is ensuring that every step of the fabrication leaves no residue on the surface, as even monolayer levels of contamination could significantly reduce photoelectron transmission and beam brightness.

In the first step of fabrication, commercial two-dimensional materials, which are grown on a copper foil, are coated with a thin gold layer in the CVC SC4500 thermal/e-beam evaporator. The two-dimensional material on the backside of the copper foil is then removed using 100W of oxygen plasma in the YES oxygen plasma asher. The copper foil is then removed with an aqueous etchant, allowing the graphene side of the gold-coated graphene to be adhered to a low energy substrate. The gold film is then removed by a second aqueous etch.

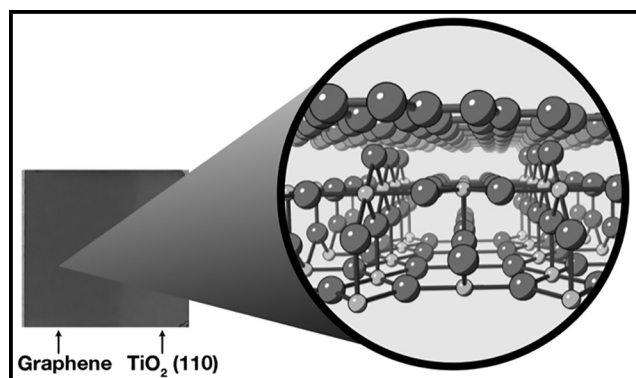


Figure 1: Optical image of TiO₂(110) with single-layer graphene on left side. The inset is a model of single-layer graphene on TiO₂(110).

Fabricating Planar Microwave Resonators for On-Chip Electron Spin Resonance Spectroscopy

CNF Project Number: 2705-18

Principal Investigator(s): Farhan Rana

User(s): Arjan Singh

Affiliation(s): Electrical and Computer Engineering, Cornell University

Primary Source(s) of Research Funding: Air Force Research Lab (AFRL) Grant No. FA9550-18-1-0529

Contact(s): farhan.rana@cornell.edu, as2995@cornell.edu

Primary CNF Tools Used: AJA sputter deposition tool, CVC SC4500 odd/even evaporator, copper electroplating hood, Logitech Orbis chemical-mechanical-polisher (CMP)

Abstract:

Electron spin resonance (ESR) spectroscopy has been a useful tool for measuring defect spins in semiconductors [1-6]. We are utilizing the robust capabilities of the Cornell NanoScale Facility (CNF) to develop an ESR spectrometer with the capability to measure defect spins in MBE-grown films as thin as 100 nm. Here, we demonstrate a planar microwave resonator, the principal device to be used in the spectrometer, with an internal Q -factor over 150 at ~ 10 GHz, fabricated completely at CNF. We use a unique “photoresist-mold-defined” fabrication process to pattern copper thicker than $5 \mu\text{m}$.

Summary of Research:

Electron spin resonance (ESR) spectroscopy is based on exploiting the Zeeman interaction between a magnetic field and a spin. Ever since it was proposed to study nuclear spins nearly a century ago [8], it has been a useful tool to study spins in materials [1-7].

A (non-oscillating) magnetic field splits degenerate spin states by an energy, $E = \gamma_s B$ (assuming spin-1/2 particles), where γ_s is the gyromagnetic ratio (the ratio between the magnetic moment of a particle to its angular momentum) and B is the applied magnetic field. The energy E for magnetic fields on the order of 1 T can easily be supplied by microwaves of frequencies, $f \sim 1$ -10 GHz.

Thus, the essential idea of ESR spectroscopy is that by supplying microwave radiation to semiconductor samples subject to a magnetic field, we can induce transitions between spin states of defects when the condition, $hf = \gamma_s B$ is met, where h is Planck's constant.

By observing these transitions, we can extract the gyromagnetic ratio, γ_s , associated with a defect-spin state, giving us insight into its electrical/magnetic properties. Figure 1 shows a schematic of such an ESR experiment.

ESR spectrometers, by and large, use a 3-D microwave resonator to deliver microwaves to samples subject to a DC magnetic field. 3-D microwave resonators, owing to their large magnetic field mode volumes, are not sensitive to MBE grown thin films. Using a 2-D, planar microwave resonator we can minimize the magnetic field mode volume, and thus minimize the magnetic field fill factor (represents the fraction of magnetic field seen by the film being probed). A small magnetic fill factor (close to unity) will allow us to probe defect spins in semiconductor films as thin as ~ 100 nm. However, the small mode volume of a 2-D planar resonator also means, that much of the magnetic field is within the substrate on which the resonator is patterned. To minimize the dielectric loss resulting from this, we use a sapphire substrate, owing to sapphire's small loss-tangent and high dielectric constant. To minimize the conductor loss, we use thick copper ($\sim 5 \mu\text{m}$) to define our resonating circuit. Figure 2 shows the experimental setup we use for ESR spectroscopy.

Methods and Results:

We used the Cornell NanoScale Facility (CNF) to fabricate this 2D resonator. Since we had to pattern copper $5 \mu\text{m}$ thick, we adopted a unique fabrication process [9], which is schematically described in Figure 3a.

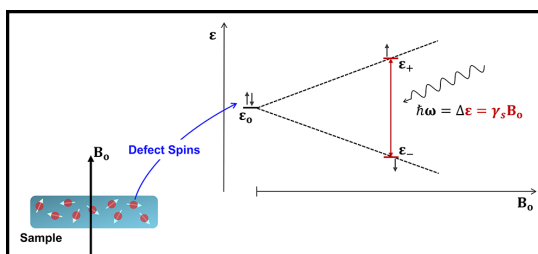


Figure 1: Schematic showing the basic principle of electron spin resonance (ESR) spectroscopy.

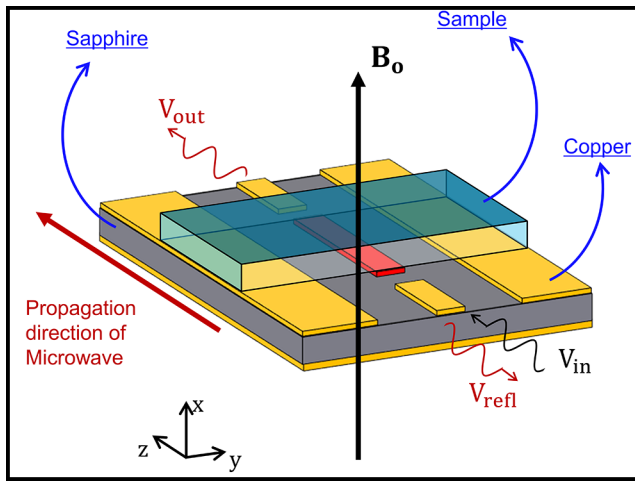


Figure 2: Basic layout of our ESR measurement. The planar microwave resonator lies at the heart of the setup and is fabricated at the Cornell NanoScale Facility (CNF).

The basic principle is as follows. (1) We first define a mold by patterning thick ($\sim 6 \mu\text{m}$) photoresist on a $600 \mu\text{m}$ sapphire substrate, using *contact photolithography*. (2) We then deposit a thin ($\sim 80 \text{ nm}$) film of platinum using the *sputter deposition tool*. (3) This platinum film serves as the seed to then *electroplate* $\sim 8 \mu\text{m}$ of copper. (4) We then use the *chemical-mechanical-polisher* (CMP) in the cleanroom to lap and polish the copper film down to $\sim 5 \mu\text{m}$ and make it smooth (roughness on the order of 10 nm). (5) Finally, we strip the photoresist, which leaves us with our patterned devices. A picture of the finished devices can be seen in Figure 3b.

Figure 4 shows the S_{21} (transmission coefficient) parameter of our device. We clearly see a sharp resonance at 10.8 GHz , which we fit using a Lorentzian lineshape. This resonance corresponds to a linewidth of 120 MHz , a loaded Q -factor of 90 , and an internal Q -factor of ~ 162 .

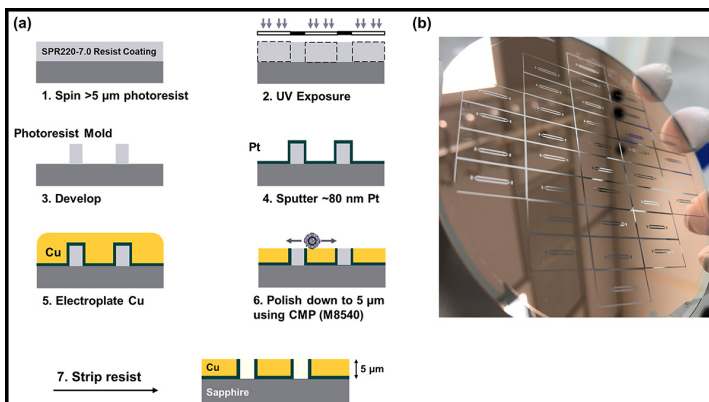


Figure 3: (a) Shows the schematic of the fabrication process used to fabricate our microwave resonator. (b) Shows the finished devices made using said process.

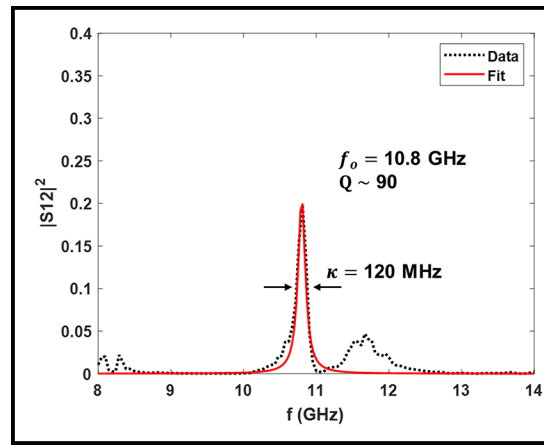


Figure 4: The S_{21} parameter (transmission coefficient) of our resonator, along with a Lorentzian fit to the data.

Conclusion and Future Steps:

This microwave characterization shows that our devices are functioning well with high quality factors. We hope to now use these devices to do ESR measurements on semiconductor thin films.

Future work at CNF will also involve fabricating devices that use a superconducting metal (niobium or aluminum), instead of copper, to define out resonators. This will allow us to reduce our conductor loss to a point that we can approach the quantum limit of spin detection [10].

Acknowledgements:

I would like to thank the CNF staff, without whom this work would not have been possible and will not be able to continue. I especially thank Chris Alpha, Aaron Windsor, Tom Pennell, Garry Bordonaro, and Jeremy Clark for their invaluable input and support.

References:

- [1] M Baeumler, et al, J. Phys. C: Solid State Phys. 20 L963 (1987).
- [2] W. E. Carlos, et al., Phys. Rev. B 48, 17878 (1993).
- [3] J H N Loubser and J A van Wyk, Rep. Prog. Phys. 41 1201 (1978).
- [4] W. V. Smith, et al., Phys. Rev. 115, 1546 (1959).
- [5] B. E. Kananen, et al., Applied Physics Letters 110, 202104 (2017).
- [6] Nguyen Tien Son, et al., Applied Physics Letters 117, 032101 (2020).
- [7] Conrad Clauss, et al., J. Phys.: Conf. Ser. 592 012146 (2015).
- [8] G. Breit and I. I. Rabi, Phys. Rev. 38, 2082 (1931).
- [9] Y. Shin, et al., Journal of Microelectromechanical Systems vol. 19, no. 3 (2010).
- [10] A. Bienfait, et al., Nature Nanotechnology, volume 11, pages 253-257 (2016).

Scissionable Polymer Photoresist for Extreme Ultraviolet Lithography

CNF Project Number: 2751-18

Principal Investigator(s): Christopher Kemper Ober

User(s): Jingyuan Deng

Affiliation(s): Materials Science and Engineering, Cornell University

Primary Source(s) of Research Funding: Intel Corporation

Contact(s): c.ober@cornell.edu, jd966@cornell.edu

Primary CNF Tools Used: ASML 300C DUV stepper, JEOL-6300 e-beam lithography, P10 profilometer

Abstract:

Extreme ultraviolet (EUV) is one of the most promising methods to create nano-size patterns below 10 nm. Numerous EUV resists have been developed in last decades to accommodate EUV lithography. The main challenge of EUV lithography lies in RLS tradeoff, which specify the tradeoff among resolution (R), line edge roughness (L) and sensitivity (S). In addition, EUV lithography suffers from low photon numbers, which may cause stochastic issues. In this work, we developed chemically amplified chain scissionable polymers to tackle these issues. Polyphthalaldehyde (PPA) based photoresists have been synthesized and their lithographic performance have been investigated.

Summary of Research:

Scissionable polymers are polymers that will depolymerize under different stimuli including acid, base, and free radicals [1]. These polymers have been investigated in the development of photoresists and other degradable materials. This work focuses on the poly(phthalaldehyde), PPA, family of scissionable polymers. The PPA backbone consists of acetal linkages that are very sensitive to acids. Upon exposure to acids, the polymer chain depolymerizes to its corresponding monomers.

This depolymerization behavior makes PPAs excellent candidates as photoresist materials. Several new architectures are being explored. For example, PPAs with tethered photoacid generators (PAGs), which release acid upon irradiation, depolymerize upon exposure followed by a post exposure bake step. The depolymerized monomers in exposed areas could be easily removed using appropriate organic solvents while the unexposed areas remain unchanged. Therefore, both unsubstituted and substituted PPAs may equally serve as a positive tone photoresist.

This study focuses on the development of low exposure dose, sensitive PPA photoresists, which do not suffer from materials stochastic issues related to non-uniformities at nanoscale present in multi-component systems for EUV lithography.

In order to improve the lithographic performance of the PPA photoresists, the structure of the polymer backbone as well as photoacid generators (PAGs) are being investigated and tailored for EUV lithography. Aryl sulfonates were prepared as non-ionic PAGs for PPA photoresists [2]. The steric and electronic nature of the aryl sulfonate PAGs can be easily tuned to optimize acid generation efficiency and their compatibility with a polymer photoresist matrix.

The homogenous solution of PPA polymers and PAGs were prepared and spin coated on a silicon wafer. The coated silicon wafers were then exposed using ASML 300C DUV stepper. After exposure, the exposed film was baked and developed.

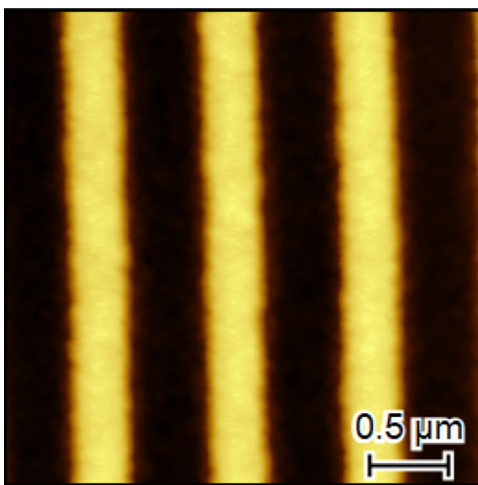


Figure 1. 1:1 Line space pattern with feature size 512 nm observed under AFM after exposure of 100mJ/cm² deep UV exposure.

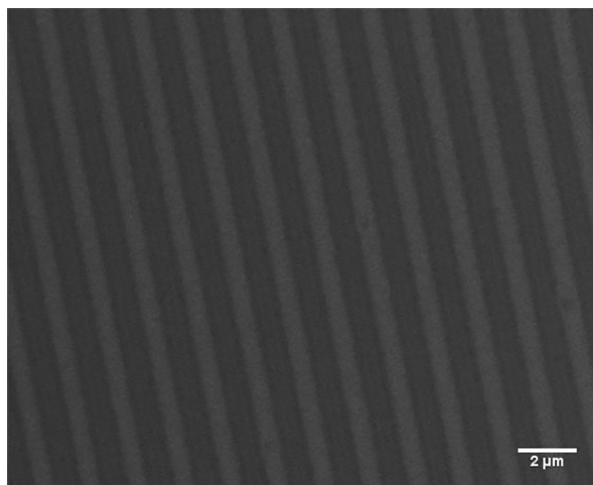


Figure 2. 1:1 Line space pattern with feature size 512 nm observed under SEM after exposure of 100mJ/cm² deep UV exposure.

Results and Discussions:

The resulting line-space patterns were characterized using AFM and SEM. The images are shown in Figure 1 and 2, respectively.

As seen from these figures, the relatively rough line edge roughness was caused by the acid diffusion, which could be alleviated by changing the chemical structure of the photoacid generator.

Next, we plan to explore the resolution limit of these photoresists with different photoacid generators using e-beam and EUV. These samples are currently under preparation.

Summary:

In summary, preliminary results were obtained with chain scissionable photoresists. With these results in hand, the lithographic performance of newly developed functionalized PPAs will be investigated under DUV, e-beam and EUV to pursue higher resolution and improved LER.

References:

- [1] Yardley, R. E.; Kenaree, A. R.; Gillies, E. R. *Macromolecules* 2019, 52, 6342.
- [2] Sulc, R.; Blackwell, J. M.; Younkin, T. R.; Putna, E. S.; Esswein, K.; DiPasquale, A. G.; Callahan, R.; Tsubaki, H.; Tsuchihashi, T. *Proc. SPIE*, 2009; 7273, 72733.

Control of Water Adsorption via Electrically Doped Graphene

CNF Project Number: 2767-19

Principal Investigator(s): Scott Schiffres

User(s): Morteza H. Bagheri, Rebecca T. Loibl

Affiliation(s): Department of Mechanical Engineering, Binghamton University, State University of New York, Binghamton, NY 13902, USA; Materials Science and Engineering Program, Binghamton University, State University of New York, Binghamton, NY 13902, USA

Primary Source(s) of Research Funding: State University of New York at Binghamton's Transdisciplinary Area of Excellence Seed Grant, State University of New York Startup Funds, National Science Foundation Award 1846157

Contact(s): sschiff@binghamton.edu, mortezahb@binghamton.edu

Website: <http://ws.binghamton.edu/schiffres/>

Primary CNF Tools Used: Oxford ALD FlexAL, CVC SC4500 odd/even evaporator, YES asher

Abstract:

The interaction of graphene with water molecules under an applied electric field is not thoroughly understood, yet this interaction is important to many thermal, fluidic, and electrical applications of graphene. In this work, the effect of electrical doping of graphene on water adsorption was studied through adsorption isotherms and current-voltage (IV) characterizations as a function of the Fermi level. The water adsorption onto graphene increased $\sim 15\%$ and the doping levels increased by a factor of three with a gate-to-graphene voltage of +20 or -20V compared to 0V for sub-monolayer adsorption. This change in uptake is attributed to the increase in density of state of graphene upon electrical-doping, which changes the Coulombic and van der Waals interactions. The water adsorption onto graphene is either *n*- or *p*-doping depending on the applied gate-to-graphene voltage. The ambi-doping nature of water onto graphene is due to the polar nature of water molecules, so the doping depends on the orientation of the water molecules.

Summary of Research:

Being extremely thin and thermally stable, graphene is an appealing method of surface modification [1-3]. It has been noted that water adsorption onto a supported graphene changes graphene's electronic structure. However, how water adsorption changes with altering the graphene Fermi level has never been studied experimentally [4].

We set out to test the hypothesis that the water adsorption behavior onto graphene can be tuned by electrically shifting the Fermi level, and hence the energetics of adsorption. In order to test this hypothesis, water adsorption onto back-gated graphene field effect transistors (GFETs) was studied as a function of electrical-doping via a quartz crystal microbalance (QCM) and current-voltage (IV) curve measurements.

Back-gate GFETs were fabricated onto 5 MHz AT-cut QCMs. An adhesion layer, 100 nm of Ti, was deposited onto the top electrode of the QCM via e-beam evaporation (AJA International). A 100 nm Al_2O_3 was deposited via atomic layer deposition (ALD) with trimethylaluminum (TMA) and oxygen plasma at 200°C (Oxford Flex AL) to form the dielectric onto the QCM.

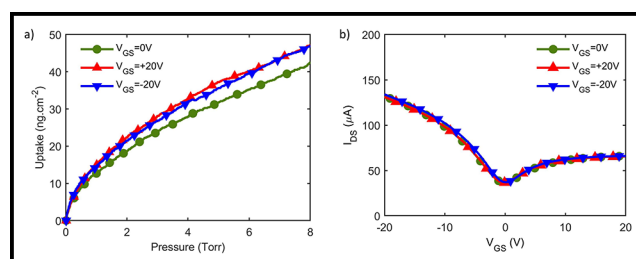


Figure 1: Adsorption isotherms were measured in an environmental vacuum chamber using the shift in the resonance frequency of the QCM upon water vapor exposure. (a) Shows the adsorption isotherms of water onto graphene for three different gate voltages: 0V, +20V, and -20V. (b) The three applied gate voltages during water adsorption induced no doping, n-doping, and p-doping, respectively.

Then, PMMA-backed CVD graphene was transferred onto the QCM. After the PMMA removal, the source and drain (5 nm Cr / 100 nm Au) were deposited on top of graphene via e-beam evaporation (AJA International), creating a 7.1 mm × 7.1 mm channel.

Adsorption isotherms were measured in an environmental vacuum chamber using the shift in the resonance frequency of the QCM upon water vapor exposure. Figure 1a shows the adsorption isotherms of water onto graphene for three different gate voltages: 0V, +20V, and -20V. The three applied gate voltages during water adsorption induced no doping, *n*-doping, and *p*-doping, respectively (Figure 1b). It can be seen in Figure 1a that the non-zero-gate voltages led to higher uptakes. However, switching the gate voltage polarity resulted in similar uptakes.

This change in uptake for the doped graphene is attributed to the change in the Coulombic and van der Waals interactions due to the increase in density of state (DOS) of graphene upon doping [5].

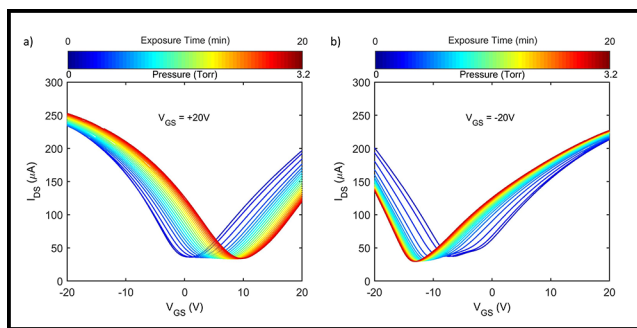


Figure 2: The IV curves after water vapor exposure with different applied gate voltages. (a) The adsorption of water molecules shifted the V_{CNP} in the positive direction and made the graphene less *n*-doped. (b) The adsorption of water molecules moved the V_{CNP} in the negative direction and made the graphene less *p*-doped.

In a different set of experiments, IV scans were periodically conducted after x minutes of water vapor exposure ($x = 0, 1, 2, \dots, 20$). Figure 2 shows the IV curves after water vapor exposure with different applied gate voltages.

During the adsorption with an applied gate voltage of +20V, the graphene was initially *n*-doped; however, the adsorption of water molecules shifted the V_{CNP} in the positive direction and made the graphene less *n*-doped (Figure 2a), i.e., water adsorption induced holes in graphene. On the other hand, when the applied gate voltage was kept at -20V during adsorption, the graphene was initially *p*-doped; however, the adsorption of water molecules moved the V_{CNP} in the negative direction and made the graphene less *p*-doped (Figure 2b), i.e., water adsorption induced electrons in graphene.

When the applied gate voltage (V_{GS}) is greater than the V_{CNP} , electrons are the dominant charge carriers in graphene, so that water molecules tend to adsorb onto graphene with the positive side of the dipole (the H atoms) towards graphene. This creates a dipole layer of water molecules with their positive charge next to the graphene that induces *p*-doping. Figure 2a supports this hypothesis, as when $V_{GS} = +20V$ was greater than V_{CNP} , the V_{CNP} shifted in the positive direction, which indicates water is *p*-doping graphene.

Conversely, when the gate voltage is less than the V_{CNP} , the water molecules adsorb onto graphene with their negative charges toward the graphene (the OH bonds upward), which creates a dipole layer of water molecules and induces *n*-doping. This agrees with Figure 2b, where $V_{GS} = -20V$ was less than V_{CNP} , and the V_{CNP} shifted in the negative direction, which indicates water is *n*-doping graphene (Figure 3).

A detailed discussion of this research can be found at Ref 4.

References:

- [1] Rafiee, J.; Mi, X.; Gullapalli, H.; Thomas, A. V.; Yavari, F.; Shi, Y.; Ajayan, P. M.; Koratkar, N. A. Wetting Transparency of Graphene. *Nat. Mater.* 2012, 11 (3), 217-222. <https://doi.org/10.1038/nmat3228>.
- [2] Preston, D. J.; Mafra, D. L.; Miljkovic, N.; Kong, J.; Wang, E. N. Scalable Graphene Coatings for Enhanced Condensation Heat Transfer. *Nano Lett.* 2015, 15 (5), 2902-2909. <https://doi.org/10.1021/nl504628s>.
- [3] Bagheri, M. H.; Loibl, R. T.; Boscoboinik, J. A.; Schiffrès, S. N. Adsorption Transparency of Supported Graphene. *Carbon* 2019, 155, 580-586. <https://doi.org/10.1016/j.carbon.2019.08.083>.
- [4] Bagheri, M. H.; Loibl, R. T.; Schiffrès, S. N. Control of Water Adsorption via Electrically Doped Graphene: Effect of Fermi Level on Uptake and H₂O Orientation. *Adv. Mater. Interfaces* n/a (n/a), 2100445. <https://doi.org/10.1002/admi.202100445>.
- [5] Hong, G.; Han, Y.; Schutzius, T. M.; Wang, Y.; Pan, Y.; Hu, M.; Jie, J.; Sharma, C. S.; Müller, U.; Poulidakos, D. On the Mechanism of Hydrophilicity of Graphene. *Nano Lett.* 2016, 16 (7), 4447-4453. <https://doi.org/10.1021/acs.nanolett.6b01594>.

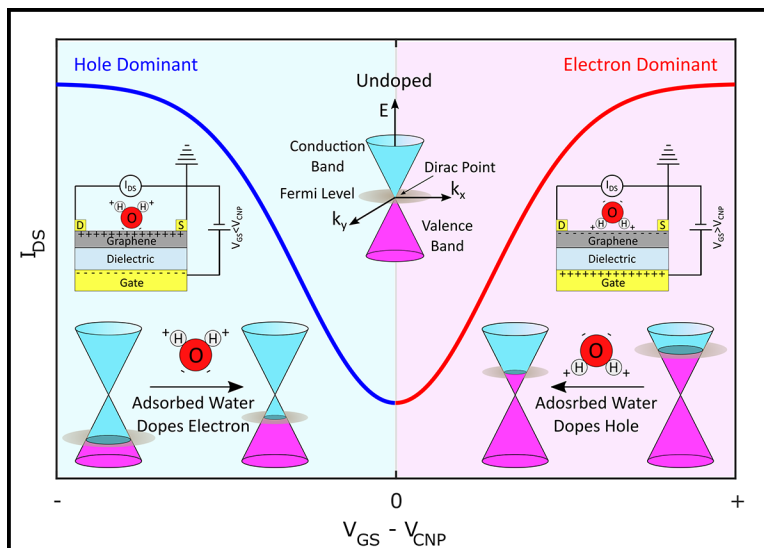


Figure 3: $V_{GS} = -20V$ was less than V_{CNP} and the V_{CNP} shifted in the negative direction, which indicates water is *n*-doping graphene.

Driving Structure Selection in Colloidal Particles Through Confinement

CNF Project Number: 2794-19

Principal Investigator(s): Julia Dshemuchadse

User(s): Rachael S. Skye

Affiliation(s): Department of Materials Science and Engineering, Cornell University

Primary Source(s) of Research Funding: National Science Foundation

Graduate Research Fellowship under Grant No. DGE-1650441

Contact(s): jd732@cornell.edu, rss364@cornell.edu

Primary CNF Tools Used: CNF Computer Cluster

Abstract:

We use Monte Carlo simulations of hard tetrahedral particles to examine the effects of external confinement and particle shape on the self-assembly process. We examine a set of particles related to tetrahedra by vertex truncation. Through simulating self-assembly in a spherical container, we show that confined tetrahedral particles assemble in distinct concentric shells up to hundreds of particles. We also show that the curvature of the container can drive the local environment of particles towards specific motifs, allowing researchers to selectively induce the self-assembly of particular structures.

Summary of Research:

This work uses numerical simulations to explore the effect of confinement on the self-assembly behavior of hard colloidal particles — in particular tetrahedral particles. In experiment, advancements in synthesis of anisotropic particles have allowed the development of an array of shaped nanoparticles [1]. This raises the question: what structures do these different shapes assemble?

Computational studies enable the exploration of the bulk behavior of particles with different shapes [2], replicating, for example, an experiment with particles floating in solution. However, the non-bulk case is less well explored. Here, we investigate the behavior of hard (non-attractive) tetrahedral particles confined in spherical walls, and the effects of wall curvature and particle shape on interparticle motifs. In experiment, this mimics assembly mechanisms such as confinement in an evaporating droplet [3].

To explore shape space, we apply vertex truncation to hard tetrahedra. Three shapes were given particular attention: the Platonic tetrahedron, the Archimedean truncated tetrahedron (ATT), and the space-filling truncated tetrahedron (STT). These shapes mark different regions in self-assembly space: the Platonic tetrahedra assemble a dodecagonal quasicrystal, the ATTs a diamond-type crystal, and the STTs lie on the boundary between the two structures, in a region of

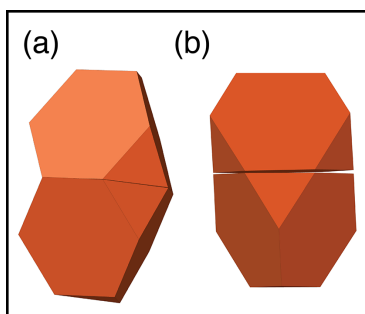


Figure 1: (a) The aligned motif (ca. 70.5°) vs. (b) the anti-aligned motif (90°).

structural competition [4]. We use a continually shrinking, hard spherical wall, compressed to high pressure to induce assembly. Simulations were performed with the HOOMD-blue Hard-Particle Monte Carlo (HPMC) package [5-7], using the resources provided by the CNF Computer Cluster, among others.

To explore the effects of container size — and therefore curvature — at equal pressure, we increase the number of particles in the system. We observe that concentric shells of particles form, conforming to the curvature of the wall. At small N , the vertices cluster in the center. Additional particles are added in the outer shell until the container is large enough that a two-shell structure forms. We have shown that this process repeats for a third shell, and organization into distinct layers continues up to thousands of particles.

The core-shell structure drives the particles towards local motifs that conform to the container wall. In tetrahedral particles, there are two dominant motifs, characterized by their misorientation angle: the angle through which a particle must be rotated in order to match the orientation of a reference particle. For tetrahedral particles, there are two important local motifs, both with facet-to-facet alignment (Figure 1): in one motif, the vertices of both particles align with one another (misorientation angle = ca. 70.5°), while in

the second motif, the vertices of one particle align with the edge midpoints of the other (misorientation angle = 90°) [8]. The “anti-aligned” misorientation angle is characteristic of a diamond-type structure formed in the bulk by ATTs, whereas Platonic tetrahedra favor the “aligned” motif, characteristic of a dodecagonal quasicrystal.

Plotting the change in predominant motif as the system size increases gives information on how the container drives the assembled structure. At small N , the clustering of vertices near the center of the containers drives the particle motif towards aligned for all shapes. For Platonic tetrahedra, the bulk motif is identical, so there is no overall transition with increasing N (Figure 2a).

In contrast, the ATT bulk motif is anti-aligned, leading to a gradual transition in which the frequency of the anti-aligned motif increases and the aligned motif decreases (Figure 2c). The intermediate shape — STT — lies in a region that exhibits both aligned and anti-aligned motifs in the bulk.

In confined systems, we see first an increase in the frequency of the anti-aligned motif, followed by a decrease towards the bulk system, again persisting up to thousands of particles (Figure 2c). By mapping where different motifs occur, we see that in very large containers, the anti-aligned motif is clustered near the surface. This indicates that low-curvature walls favor the diamond-type structure.

Conclusions and Future Steps:

We have shown that it is possible to influence structure selection through changing the curvature of the walls of confined systems, driving assembly towards desirable structures. Going forward, we intend to study the effects of other confinement geometries.

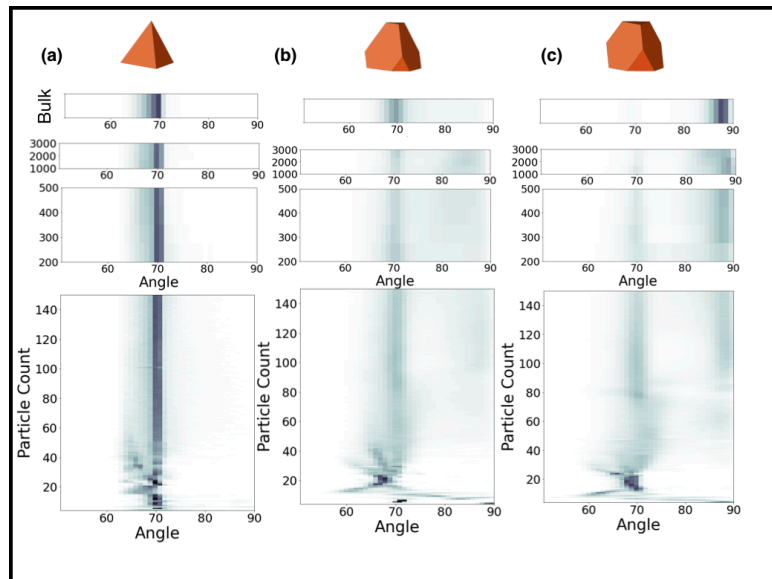


Figure 2: The distribution of misorientation angles for (a) Platonic tetrahedra, (b) space-filling truncated tetrahedra, and (c) Archimedean truncated tetrahedra with increasing container size. Color intensity corresponds to the frequency of that angle.

References:

- [1] J. Henzie, M. Grünwald, A. Widmer-Cooper, P. L. Geissler, P. Yang, *Nature Materials* 11, 131-137 (2012).
- [2] P. F. Damasceno, M. Engel, S. C. Glotzer, *Science* 33, 453-457 (2012).
- [3] B. de Nijs, S. Dussi, F. Smalenburg, J. D. Meeldijk, D. J. Groenendijk, A. Imhof, L. Fillion, A. van Blaaderen, M. Dijkstra, *Nature Materials* 14, 56-60 (2015).
- [4] D. Klotsa, E. R. Chen, M. Engel, S. C. Glotzer, *Soft Matter* 14, 8692-8697 (2018).
- [5] J. A. Anderson, C. D. Lorenz, A. Travasset, *Journal of Computational Physics* 227, 5342-5359 (2008).
- [6] J. Glaser, T. D. Nguyen, J. A. Anderson, P. Lui, F. Spiga, J. A. Millan, D. C. Morse, S. C. Glotzer, *Computer Physics Communications* 192, 97-107 (2015).
- [7] J. A. Anderson, M. E. Irrgang, S. C. Glotzer, *Computer Physics Communications* 204, 21-30 (2016).
- [8] E. G. Teich, G. van Anders, S. C. Glotzer, *Nature Communications* 10, 64 (2019).

Elucidating the Chemical Crypsis Mechanism in South African Snakes by Determining Microscale and Nanoscale Structure-Function Relationships in Snake Skin Sheds and Replicas

CNF Project Number: 2819-19

Principal Investigator(s): Robert Shepherd

User(s): Rachel Miller

Affiliation(s): Materials Science and Engineering, Cornell University

Primary Source(s) of Research Funding: National Science Foundation, Contract: EFMA-1830924

Contact(s): rfs247@cornell.edu, rm973@cornell.edu

Website: orl.mae.cornell.edu

Primary CNF Tools Used: NanoScribe GT2

Abstract:

Humans have been studying and mimicking animal's visual crypsis using wearable camouflage since the 18th century. Yet, only recently we have documented and attempted to understand the origins of chemical crypsis, the ability to become imperceptible to olfaction. Specifically this work aims to elucidate the mechanism of chemical crypsis in the first vertebrate shown to exhibit this trait, a snake known as the Puff adder (*Bitis arietans*).

The major feature distinguishing the Puff adder from its non-cryptic brethren such as the Night adder (*Causus rhombeatus*) is the skin surface structure. The skin's micron-scale, high aspect ratio, curved features known as 'fingers' create an array of wells for odorants to pool, significantly reducing odorant volatility and therefore rendering the Puff adder imperceptible to smell. To study and quantify this phenomena independent of snakeskin material, snakeskin surface biomes, and environmental contaminants, we employ various imaging and 3D printing processes to create a variety of detailed and accurate scaled models of both the puff adder skin and night adder skins. Nano-focused computed tomography (nano-CT) is used to create three-dimensional renderings of skins. To maximize accuracy of replicas, nano-CT image segmentation is informed by focused ion beam (FIB) and scanning electron microscopy (SEM) images. These digitally rendered surfaces are printed in epoxy using 3D printing, requiring the use of two photon polymerization (2PP) on the NanoScribe GT2 for micron-scale feature resolution.

We show the use of 2D Fourier transform analysis sequentially along the long axis as a means to quantify periodicity and investigate the degree of quasi-ordered orientation as a predictor for surface thermodynamic phenomena. Physical experiments on printed models and topographical analysis of digital renderings are used together to analyze and quantify the effects of structure periodicity and surface-area-to volume ratio on adhesion, wetting, and evaporation.

Summary of Research:

It has been shown that many snakes may actually hide not in plain sight using visual camouflage, but instead in plain "smell". Instead of being visually cryptic, these South African snakes are chemically cryptic [2]. Specifically, work done by A.K. Miller et al demonstrates that the Puff adder relies on chemical crypsis in order to effectively ambush its prey [1]. Extensive behavioral studies by A.K. Miller et al have suggested that additionally, current unpublished work by A.K. Miller is showing that many snakes in South Africa and the surrounding region also are chemically cryptic.

Previously, Puff adder skins have also been noticed for their microornamentation. Their skins have high aspect ratio "fingers" that protrude out from the skin base. It has been proposed that these types of ornamentation on a similar species were used to create optical effects in the skin. Snakeskin is home to large amounts of bacteria and other odorant producing biota. We hypothesize that these skins are not chemically cryptic because of their lack of odorants, but rather because there is a structure to their skin that keeps odorants from vaporizing and being detected by predators,

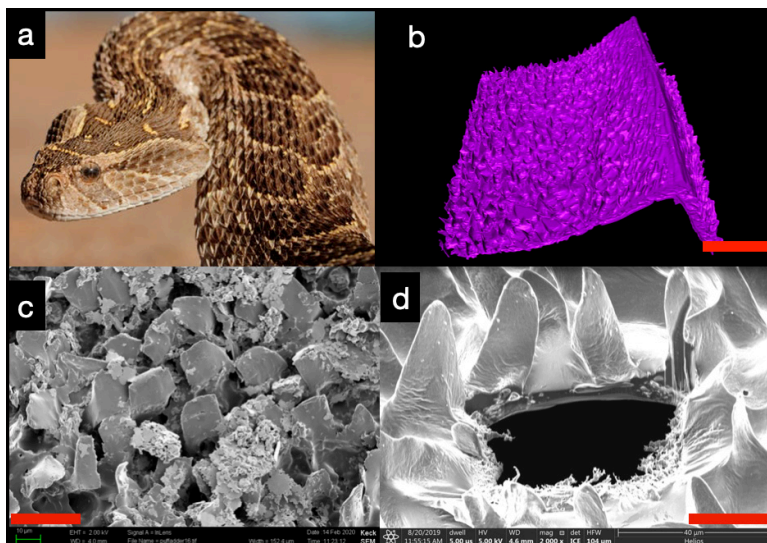


Figure 1: (a) *Bitis arietans* (Puff adder), chemically cryptic snake1. (b) Nano CT scan reconstruction of Puff adder skin section with 'fingers,' Scale bar = 100 μm . (c) SEM image of puff adder skin to show pores are more visible than in CT or FIB, Scale bar = 20 μm . (d) FIB image of Puff adder skin. Further reveals structure of 'fingers' on skin, Scale bar = 20 μm .

prey, or even mates. The high aspect ratio features on Puff adder skin creates an environment on the surface of snake skin which decreases the volatility of odorants, rendering them chemically cryptic.

Using imaging techniques — including but not limited to nano-focused X-ray computed tomography (nano-CT) (Figure 1b), scanning electron microscopy (SEM) (Figure 1c), and focused ion beam microscopy — further reveals structures of 'fingers' on skin (Figure 1d, scale bar = 20 μm (FIB), and we can comprehensively probe Puff adder skin sheds. Together these techniques enable us to render and fabricate accurate digital and physical 3D renderings of skin features via nanoscopic 3D printing on the NanoScribe Photonic Professional GT2 (Figure 2).

Conclusions and Future Work:

We have successfully created 0.1 cm \times 0.1 cm footprint 1:1 Puff adder skin replica prints with submicron scale resolution using the NanoScribe GT2 printing apparatus (Figure 2). Nanoscopic prints and snakeskin sheds will serve as masters for replica molding, the former being non-destructive technique and the latter being a destructive technique.

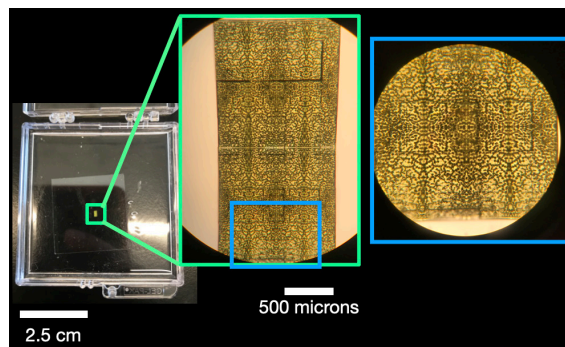


Figure 2: 2PP 3D printed Puff adder snakeskin replicas, photograph and optical microscope images.

Chemical treatment of these nano- and microscale features will be performed using thiolate mediated self-assembled monolayer chemistry, with a final test to be performed using modified substrates that chemically mimic the original skin.

To test these structures' impact on odorant volatility it would be beneficial to be able to fabricate consistent, large area replicas of these features. This could potentially involve reactive ion etching to achieve high aspect ratio features or wet etching methods, depending on the material chosen for these replicas. It is currently being debated as to whether or not it is possible to make these replica structures out of materials that are not silicone, epoxy, or other commercial plastics and instead out of keratin itself or another functionally and/or structurally similar material.

References:

- [1] McKay S, Glaudas X, Alexander GJ, Miller AK, Maritz B. An ambusher's arsenal: chemical crypsis in the puff adder (*Bitis arietans*). *Proceedings of the Royal Society B*, 282, 2015.
- [2] Graeme D Ruxton. Non-visual crypsis: a review of the empirical evidence for camouflage to senses other than vision. *Philosophical Transactions of The Royal Society*, 364(1516), 2008.